









# Circumgalactic Gas at Its Extreme: Tidal Gas Streams around the Whale Galaxy NGC 4631 Explored with *HST/COS*

P. Richter<sup>1</sup> , B. Winkel<sup>2</sup> , B. P. Wakker<sup>3</sup> , N. M. Pingel<sup>4,5</sup>, A. J. Fox<sup>6</sup> , G. Heald<sup>7</sup>, R. A. M. Walterbos<sup>8</sup> , C. Fechner<sup>1</sup>, N. Ben Bekhti<sup>9</sup>, G. Gentile<sup>10</sup>, and L. Zschaechner<sup>11,12</sup> 

<sup>1</sup> Institut für Physik und Astronomie, Universität Potsdam, Karl-Liebknecht-Str. 24/25, D-14476 Golm, Germany

<sup>2</sup> Max-Planck-Institut für Radioastronomie (MPIfR), Auf dem Hügel 69, D-53121 Bonn, Germany

<sup>3</sup> Supported by NASA/NSF, affiliated with the Department of Astronomy, University of Wisconsin-Madison, 475 North Charter Street, Madison, WI 53706, USA

<sup>4</sup> Department of Physics and Astronomy, West Virginia University, White Hall, Box 6315, Morgantown, WV 26506, USA

<sup>5</sup> Center for Gravitational Waves and Cosmology, West Virginia University, Chestnut Ridge Research Building, Morgantown, WV 26505, USA

<sup>6</sup> Space Telescope Science Institute, 3700 San Martin Drive, Baltimore, MD 21218, USA

<sup>7</sup> CSIRO Astronomy and Space Science, P.O. Box 1130, Bentley WA 6102, Australia

<sup>8</sup> Department of Astronomy, New Mexico State University, P.O. Box 30001, MSC 4500, Las Cruces, NM 88003, USA

<sup>9</sup> Fraunhofer Institute for High Frequency Physics and Radar Techniques FHR, Fraunhoferstr. 20, D-53343 Wachtberg, Germany

<sup>10</sup> Department of Physics and Astrophysics, Vrije Universiteit Brussel, Pleinlaan 2, B-1050 Brussels, Belgium

<sup>11</sup> University of Helsinki, Physicum, Helsingin Yliopisto, Gustaf Hällströmin katu 2, FI-00560 Helsinki, Finland

<sup>12</sup> Finnish Center for Astronomy with ESO, FI-20014 Turun yliopisto, Finland

Received 2018 July 23; revised 2018 September 28; accepted 2018 October 12; published 2018 November 29

## Abstract

We present a detailed analysis of the absorption properties of one of the tidal gas streams around the “Whale” galaxy NGC 4631 in the direction of the quasar 2MASS J12421031+3214268. Our study is based on ultraviolet spectral data obtained with the Cosmic Origins Spectrograph (COS) on board the *Hubble Space Telescope* (*HST*) and 21cm-data from the HALOGAS project and the Green Bank Telescope (GBT). We detect strong H I Ly $\alpha$  absorption in the velocity range +550 to +800 km s<sup>-1</sup> related to gas from a NGC 4631 tidal stream known as Spur 2. We measure a column density of  $\log(N(\text{H I}/\text{cm}^{-2})) = 18.68 \pm 0.15$ , indicating that the quasar sightline traces the outer boundary of Spur 2 as seen in the 21 cm data. Metal absorption in Spur 2 is detected in the lines of O I, C II, Si II, and Si III in a complex absorption pattern that reflects the multiphase nature of the gas. We find that the average neutral gas fraction in Spur 2 toward 2MASS J12421031+3214268 is only 14%. This implies that ionized gas dominates the total mass of Spur 2, which then may comprise more than  $10^9 M_{\odot}$ . No significant depletion of Si is observed, showing that Spur 2 does not contain significant amounts of dust. From the measured O I/H I column density ratio, we determine an  $\alpha$  abundance in Spur 2 of  $0.13_{-0.05}^{+0.07}$  solar ( $[\alpha/\text{H}] = -0.90 \pm 0.16$ ), which is substantially lower than what is observed in the NGC 4631 disk. The low metallicity and low dust content suggest that Spur 2 represents metal-deficient gas stripped off a gas-rich satellite galaxy during a recent encounter with NGC 4631.

**Key words:** galaxies: evolution – galaxies: halos – galaxies: interactions – ISM: abundances – quasars: absorption lines

## 1. Introduction

Galaxy evolution at low and high redshift is believed to be largely influenced by the galaxies’ interactions with their immediate cosmological environment. As most galaxies are expected to consume their interstellar gas content on relatively short timescales to sustain star formation, the inflow of gas from outside belongs to the particularly interesting processes that are believed to strongly influence a galaxy’s star formation rate and its evolutionary state (e.g., Daveé et al. 2012). Indeed, recent observational and theoretical studies have demonstrated that the inflow of gaseous material from the intergalactic medium (IGM) and the recycling of previously expelled gas adds significantly to today’s reservoir of baryonic matter in a galaxy, thus founding the basis for future star formation activity (see recent reviews by Finlator 2017; Kacprzak 2017; Sánchez-Almeida 2017, and references therein).

In addition to IGM accretion and gas recycling, the gravitational interaction of galaxies (including minor and major mergers) represents yet another important mechanism by which galaxies acquire gas. Merger processes can deposit huge amounts of gaseous material in the form of tidal streams into the circumgalactic region around interacting galaxies long

before the main stellar bodies of the galaxies are in close proximity (Fraternali & Binney 2008; Di Teodoro & Fraternali 2014). Furthermore, because the gravitational interaction also pulls out gas from the inner-most regions of the merging galaxies, tidal gas streams often contain large amounts of neutral gas, visible at low redshift in the 21 cm emission line of neutral hydrogen and (at low and high redshifts) in damped absorption in the Ly $\alpha$  line at 1215.7 Å.

The most prominent local example for a massive tidal gas stream is the Magellanic Stream in the halo of the Milky Way, which originates in the gravitational and hydrodynamical interaction between the Magellanic Clouds and the Milky Way (e.g., Gardiner & Noguchi 1996; Connors et al. 2006; Besla et al. 2010, 2012; Nidever et al. 2010; Diaz & Bekki 2011, 2012; Salem et al. 2015; D’Onghia & Fox 2016). Recent absorption-line observations (Fox et al. 2013, 2014, 2018; Richter et al. 2013, 2018) and emission-line observations (Barger et al. 2013) indicate that the Magellanic Stream, when considered together with the Leading Arm and the Magellanic Bridge between the Large and the Small Magellanic Cloud, probably contains more than  $3 \times 10^9 M_{\odot}$  of (mostly ionized) gas, thus exceeding the combined interstellar gas mass of the

two Magellanic Clouds (Brüns et al. 2005; Fox et al. 2014; Richter 2017). Other prominent examples for extended tidal gas streams visible in 21 cm emission can be seen in the M81 group (e.g., Yun et al. 1994; Chynoweth et al. 2008) and in the “Whale” galaxy NGC 4631 (Rand 1994), the latter being the subject of the study presented here.

Detailed case studies of the circumgalactic medium (CGM) in nearby, merging galaxies hold the prospect of improving our understanding of the role of galaxy interactions for the distribution and physical properties of circumgalactic gas in the general context of galaxy evolution. To reliably estimate the chemical composition of the CGM, its distribution, its kinematics, and its total mass, the multiphase nature of the gas needs to be taken into account. For this, the combination of deep 21 cm observations (tracing neutral hydrogen gas and its spatial distribution) and high signal-to-noise (S/N) ultraviolet (UV) absorption-line measurements (tracing metal absorption in the neutral and ionized circumgalactic gas phases) offers a particularly powerful and efficient observing strategy.

In this paper, we present new UV absorption-line measurements of circumgalactic gas belonging to the tidal gas streams around the Whale galaxy NGC 4631 in the direction of the background quasar 2MASS J12421031+3214268. The quasar is located at an impact parameter of  $\rho = 40$  kpc to NGC 4631, a value that is comparable to the size of the galaxy’s HI disk (Figure 1). From the analysis of the UV data, we obtain new information on the metal and dust abundance in the southwestern part of the gaseous streams, its origin, and its total mass.

Our paper is organized as follows: in Section 2, we describe the overall properties of the tidal gas streams around NGC 4631 and summarize previous measurements. In Section 3, we outline the *HST*/COS observations, the supplementary HALO-GAS and GBT 21 cm observations, and the analysis methods. The results from the absorption-line analysis are presented in Section 4. In Section 5, we discuss the implications of our results in regard to the origin and mass of the tidal gas around NGC 4631 and compare its properties with the Magellanic Stream. Our study is summarized in Section 6.

## 2. Tidal Gas Streams around the Whale Galaxy

One particularly spectacular example for a tidal interaction between galaxies of different masses is the Whale galaxy NGC 4631 with its various companions (e.g., NGC 4656 and NGC 4627). NGC 4631 itself is a nearby ( $d = 7.4 \pm 0.2$  Mpc;  $c_z = 606$  km s<sup>-1</sup>; Radburn-Smith et al. 2011) edge-on spiral galaxy of Hubble type SB(s)d with a current star formation rate of  $2.1 M_\odot$  yr<sup>-1</sup> (Sanders et al. 2003; Kennicutt et al. 2008). It is located in a galaxy group environment containing more than a dozen galaxies (Giuricin et al. 2000). From field imaging surveys, it is known that there are plenty of dwarf satellite galaxies around NGC 4631 (Ann et al. 2011). Because most of these satellite galaxies are believed to be located within the virial radius of NGC 4631, there must be strong on-going tidal and hydrodynamical interactions between NGC 4631 and its satellite-galaxy population. The larger companion galaxies NGC 4627 and NGC 4656 are located at  $2.6'$  to the northwest and  $32'$  to the southeast of NGC 4631. Therefore, with an assumed distance of 7.4 Mpc for NGC 4631, NGC 4627, and NGC 4656 are separated by about 6 kpc and 71 kpc, respectively, from NGC 4631.

In particular, NGC 4656 is a probable candidate for a close encounter, which leads to tidal stripping of disk material, because it is massive enough to detach gas and stars from the inner regions of NGC 4631. The distorted morphology of the dwarf elliptical galaxy NGC 4627 and the well-known HI bridge between NGC 4631 and NGC 4656 (Roberts 1968; Wellichew et al. 1978; Rand 1994) are clear signs for the strong interactions between NGC 4631 and its satellite galaxies. A detailed study of the 21 cm properties of the gaseous streams around NGC 4631 was presented by Rand (1994), who grouped the various tidal features into five major spurs (see Figure 1). Combes (1978) showed that a parabolic encounter of NGC 4656 with NGC 4631 can explain part of the circumgalactic HI distribution (Spurs 1, 4 and 5). Spurs 2 and 3, on the other hand, could represent material stripped from a smaller companion of NGC 4631 (e.g., NGC 4627) or could be stirred-up material from the NGC 4631 disk from a close encounter of NGC 4631 with one of its satellites. The latter scenario is supported by the fact that Spur 2 smoothly joins onto the outer disk of NGC 4631 in the 21 cm data cube (Rand 1994).

The widespread presence of circumgalactic gas components in NGC 4631 is also indicated by a variety of other multiwavelength observations, from X-rays over H $\alpha$  to other radio wavebands (Fabbiano & Trinchieri 1987; Wang et al. 1995; Neininger & Dumke 1999; Martin & Kern 2001; Bendo et al. 2006). The detection of (hot) ionized gas far away from the galactic plane was seen as evidence that NGC 4631 drives a galactic superwind (e.g., Melo & Muñoz-Tuñón 2002; Yamasaki et al. 2009).

While the many previous observations of NGC 4631 and its environment already unveil a fascinating amount of details on the many aspects that drive the evolution of the galaxy in this complicated environment, an absorption-line study of the CGM against one or several background QSOs (essential to derive the metallicity of the gas and its total mass) has not been carried out so far. With this study, we are closing this gap.

## 3. Observations and Data Handling

### 3.1. *HST*/COS Observations and Spectral Analysis

*HST*/COS observations of the background QSO 2MASS J12421031+3214268 (alternative name: SDSS J124210.34+321427.2;  $\alpha_{2000} = 12^{\text{h}}42^{\text{m}}10^{\text{s}}.32$ ,  $\delta_{2000} = +32^{\circ}14^{\text{m}}26^{\text{s}}.80$ ,  $z_m = 1.49$ ,  $m_{\text{FUV}} = 18.78$ ) were carried out on 2016 April 19 (proposal ID: 14085; PI: P. Richter). The position of the QSO sightline with respect to the neutral gas distribution around NGC 4631 and its companion galaxies is indicated in Figure 1. As can be seen, the 2MASS J12421031+3214268 sightline passes the outer boundaries of Spur 2 south of the NGC 4631 disk.

For the COS observations, we used the G130M grating (centered on  $\lambda = 1291.0$  Å), which covers a wavelength range between 1150 and 1450 Å. The spectral resolution at the COS lifetime position 3 is  $R = 18,000$ , corresponding to a velocity resolution of 17 km s<sup>-1</sup> FWHM and a native pixel size of 3 km s<sup>-1</sup> (Green et al. 2012; Debes et al. 2016). The data for 2MASS J12421031+3214268 were collected over five *HST* orbits with a total integration time of 13.6 ks. The individual science exposures were processed with the CALCOS data reduction pipeline v3.1.7 and then coadded. For the coaddition, we used a custom-written code that aligns individual exposures

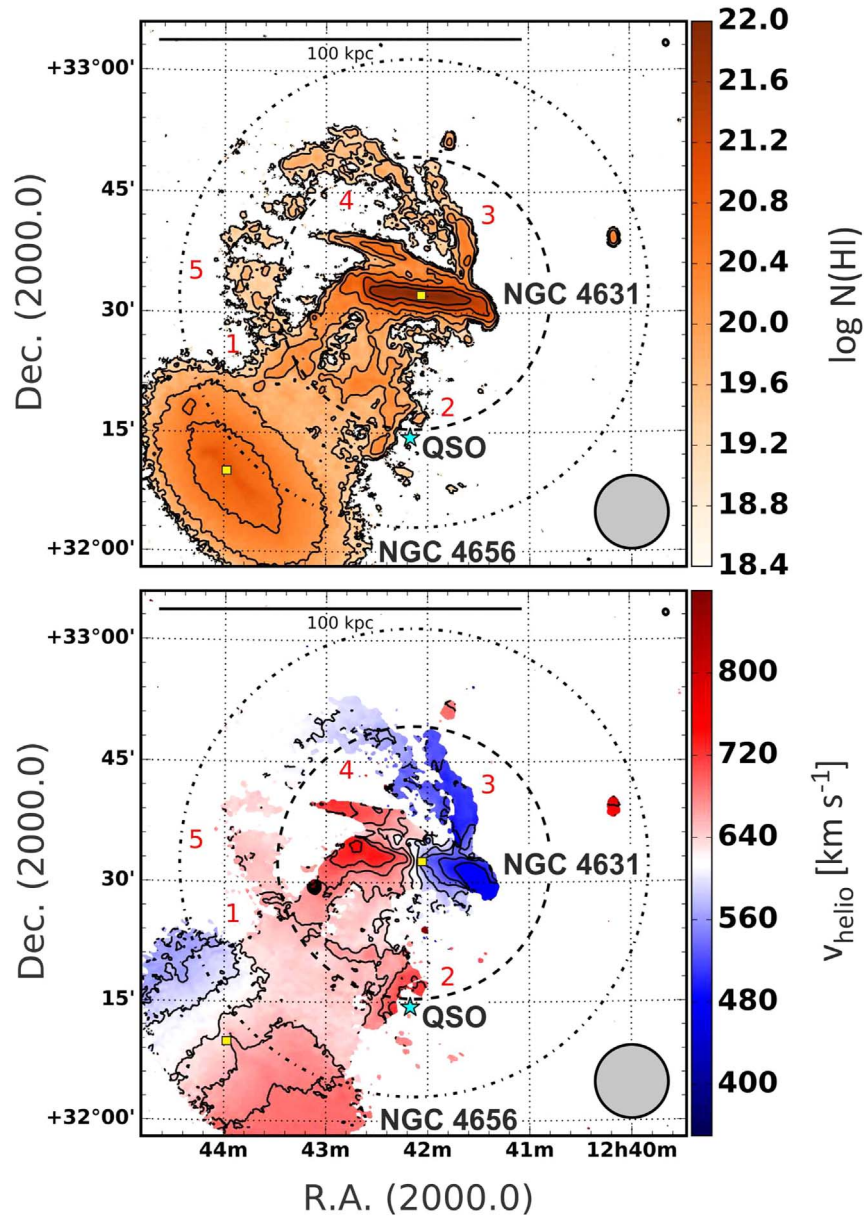


**Figure 1.** Spatial distribution of HI 21 cm emission around NGC 4631 and its neighboring galaxies from the HALOGAS/GBT observations. Upper panel: distribution of 21 cm emission with the HI column density color-coded. The HI column density contours range from  $\log N(\text{HI}) = 18.5$  to 22 in steps of 0.5 dex. Lower panel: distribution of 21 cm emission with the radial velocity color-coded. The velocity contours begin at  $+350 \text{ km s}^{-1}$ , end at  $+880 \text{ km s}^{-1}$ , and increase in increments of  $20 \text{ km s}^{-1}$ . The position of the background QSO 2MASS J12421031+3214268 is labeled with the blue star symbol. The optical center positions of NGC 4631 and NGC 4656 are indicated with the small yellow boxes. The various CGM components/spurs are labeled following the scheme presented in Rand (1994). The beam sizes appropriate for the field center and field edge are shown as gray circles in the top-right and bottom-right corners, respectively. The dashed and dotted-dashed circles indicate the 50% and 10% levels of the WSRT primary beam response (see Section 3.2).

based on a pixel/wavelength calibration that uses several ISM anchor lines (see Richter et al. 2016, 2017).

The COS G130M data cover the following strong ion transitions: H I  $\lambda 1215.7$ , C II  $\lambda 1334.5$ , N I  $\lambda 1200.7$ , O I  $\lambda 1302.2$ , Si II  $\lambda \lambda 1190.4, 1193.3, 1260.4, 1304.4$ , Si III  $\lambda 1206.5$ , Si IV  $\lambda \lambda 1393.8, 1402.8$ , P II  $\lambda 1152.8$ , S II  $\lambda 1253.8$ , and Fe II  $\lambda \lambda 1143.2, 1144.9$ . These diagnostic ion transitions trace weakly and moderately (photo)ionized gas at temperatures  $T < 10^5 \text{ K}$ . Because the important O I  $\lambda 1302.2$  line generally is contaminated by airglow lines in COS day-time data, we conducted a special reprocessing of our 2MASS J12421031+3214268 data set with night-only exposure intervals that were taken from the photon list of the individual exposures.

For the spectral analysis of the COS data, we used the span software package, which is based on the fitlyman routines implemented in ESO-MIDAS (Fontana & Ballester 1995). The span program allows us to determine equivalent widths, column densities, and Doppler parameters using either a direct pixel integration in combination with the apparent optical depth (AOD) method (Savage & Sembach 1991), a curve-of-growth method, or a Voigt-profile fitting/modeling method that takes into account the wavelength-dependent line-spread function of the spectrograph (here: COS). Wavelengths and oscillator strengths of the analyzed ion transitions were adopted from the list of Morton (2003).

Note that another, bright QSO close to NGC 4631 (SDSS J124044.68+330349.8) was also observed with COS as part of the *HST* observing program 14085. Although the *GALEX* UV magnitude is  $m_{\text{FUV}} = 18.78$ , the COS data of SDSS –J124044.68+330349.8 does not show any significant UV flux. Since the pointing was checked to be correct, this flux deficit most likely is due to a Lyman-limit system (LLS) at higher redshift. As a consequence, the COS spectrum of SDSS –J124044.68+330349.8 does not yield any usable information for our study.

### 3.2. Supplementary WSRT/HALOGAS and GBT 21 cm Data

We supplement our *HST*/COS data with 21 cm observations of NGC 4631 from the Hydrogen Accretion in LOcal Galaxies project (HALOGAS, PI: G. Heald; Heald et al. 2011). HALOGAS represents a comprehensive study of nearby galaxies using the Westerbork Synthesis Radio Telescope (WSRT). The initial goal was to perform ultra-deep HI observations of 24 nearby spiral galaxies to search for neutral gas in the circumgalactic environment of these galaxies (see Zschaechner et al. 2011; Gentile et al. 2013; Kamphuis et al. 2013 for results on individual HALOGAS galaxies). In the framework of HALOGAS, NGC 4631 was observed with the WSRT for  $10 \times 12$  hr in the “maxishort” configuration with a characteristic beam size of  $15''$  and a velocity resolution of  $\sim 4 \text{ km s}^{-1}$  (see Heald et al. 2011 for more details on the observations).

Additional 21 cm observations of the NGC 4631 environment have been carried out with the Robert C. Byrd Green Bank Telescope,<sup>13</sup> which provides an angular resolution of  $9.1'$  at 1420 MHz. The GBT data were obtained in 2014 as part of project GBT16B 293. An area of  $2 \times 2 \text{ deg}^2$  was mapped down to a theoretical column density level of  $10^{18} \text{ cm}^{-2}$  (at the GBT resolution), which corresponds to a total mapping time of 10 hr. The observational techniques used are the same as those described in Pisano (2014), while the calibration and imaging was done with the same script as in Pingel et al. (2018). Less than 0.1% of these data were flagged for RFI, then smoothed to  $6.4 \text{ km s}^{-1}$  wide velocity bins.

To combine the GBT with the WSRT data, the Common Astronomy Software Applications (CASA) task “feather” was used. A detailed description on the combination procedure is provided in the Appendix. The integrated total 21 cm column density map and the velocity field of NGC 4631 from the combined WSRT/GBT observations are shown in Figure 1 with the position of the QSO indicated with the blue star symbol. The combined data set provides a spectacular new view on the complex HI distribution in the tidal gas features around NGC 4631 and NGC 4656, complementing previous deep 21 cm observations (Weliachew et al. 1978; Rand 1994). For the interpretation of Figure 1, it is important to note that the effective angular resolution of the combined data set varies with location in the field of view.

As opposed to a mosaic, the original WSRT observations were performed with a single pointing. Because the standard reduction techniques of imaging and deconvolution of interferometer data result in a model representation of the sky multiplied by the primary-beam response of the antennas, the

true sensitivity of the native WSRT data follows the response of the primary-beam and thus decreases toward the edge of the field of view. Overplotting the 50% (dashed) and 10% (dotted–dashed) level of the primary beam response (Figure 1) according to the numerical model discussed in Heald et al. (2011) reveals that the disk of NGC 4656 is well outside the half-power response of the WSRT primary beam. Effectively, the sensitivity of the original WSRT data becomes significantly reduced toward the HI associated with NGC 4656. On the other hand, because the GBT data were obtained via multiple pointings over four square degrees, there is no variation in the sensitivity of the single dish data over the same field of view. As a result, the angular scale of the diffuse emission surrounding NGC 4656 in the combined image is almost certainly dominated by the angular resolution of the GBT data. The apparent vertical extent of the diffuse halo encompassing NGC 4646 of  $\sim 20 \text{ kpc}$  in the combined image (Figure 1) is therefore likely an upper limit.

That said, the GBT data detect almost 10 times more HI (in terms of mass) than the native WSRT data, indicating that there is extended structure that is both resolved out by the native WSRT data and missed due to the decreased sensitivity toward the companion. Additional deep 21 cm interferometer data would be very helpful to explore the full extent of diffuse 21 cm emission in the larger environment of NGC 4631 and NGC 4656.

## 4. Results

### 4.1. Metal Absorption in the COS Data

Metal absorption toward 2MASS J12421031+3214268 from Spur 2 around NGC 4631 is seen in the velocity range  $v_{\text{helio}} = +550$  to  $+800 \text{ km s}^{-1}$  in various transitions from the metal ions O I, Si II, C II, and Si III. Absorption from N I, Si IV, Fe II, and other ions is not detected.

The velocity-component structure of Milky Way plus NGC 4631 absorption toward 2MASS J12421031+3214268 between  $-300$  and  $+900 \text{ km s}^{-1}$  is shown in Figure 2 for the example of the Si III  $\lambda 1206.5$  line. Milky Way (MW) disk absorption is seen between  $v_{\text{helio}} = -90$  to  $+50 \text{ km s}^{-1}$ , while Galactic-halo absorption from a high-velocity cloud (HVC) is seen near  $-110 \text{ km s}^{-1}$ . The strong NGC 4631 absorption at  $v_{\text{helio}} = +550$  to  $+800 \text{ km s}^{-1}$  is broad and asymmetric, already indicating the presence of multiple velocity subcomponents in the gas.

In Figure 3, we display the velocity profiles of several lines from O I, Si II, C II, Si III, Si IV, and Fe II together with the 21 cm emission profile from the HALOGAS/GBT data in the range  $v_{\text{helio}} = +400$  and  $+900 \text{ km s}^{-1}$ . A double-peaked absorption profile is clearly seen in the lines of O I  $\lambda 1302.2$ , Si II  $\lambda 1193.3$ , and Si III  $\lambda 1206.5$ . The lines of C II  $\lambda 1334.5$  and Si II  $\lambda 1260.4$  at  $v_{\text{helio}} \leq +700 \text{ km s}^{-1}$  are blended by other intervening absorbers, but the two absorption components, centered at  $+660$  and  $+720 \text{ km s}^{-1}$ , still are readily visible. A precise modeling of these velocity components is presented in the next subsection.

We determined total equivalent widths,  $W_{\lambda}$ , and total logarithmic column densities,  $\log N$ , by a direct pixel integration over the velocity profiles using the apparent optical depth method (Savage & Sembach 1991). The values for  $W_{\lambda}$  and  $\log N$  derived in this manner are listed in Table 1, columns 4 and 5. In the case of nondetections, we determined upper

<sup>13</sup> The Green Bank Observatory is a facility of the National Science Foundation, operated under a cooperative agreement by Associated Universities, Inc.

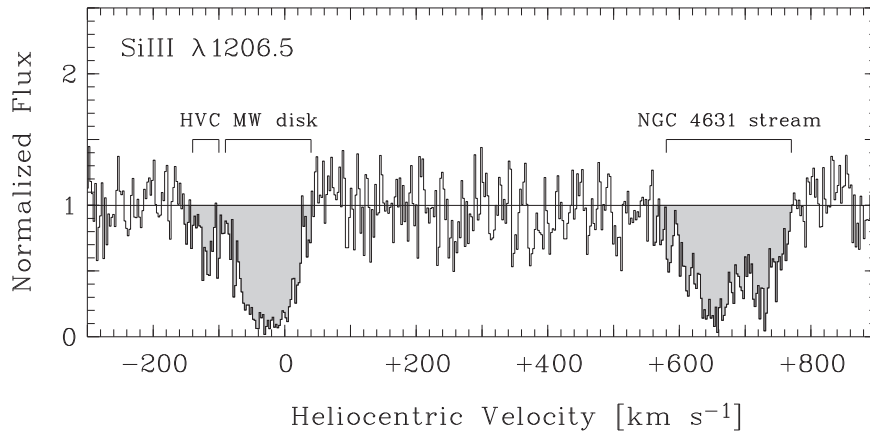


**Figure 2.** Velocity-component structure of Milky Way/NGC 4631 absorption toward 2MASS J12421031+3214268 in the Si III  $\lambda 1206.5$  line (in the heliocentric velocity frame). Milky Way absorption from the various disk and halo (high-velocity cloud; HVC) components is seen between  $-160$  and  $+60$   $\text{km s}^{-1}$ . Absorption related to the NGC 4631 tidal stream in front of the QSO is observed in the range  $v_{\text{helio}} = +550$  and  $800$   $\text{km s}^{-1}$ .

limits for  $W_\lambda$  and  $\log N$ ; for saturated lines (lines with more than 50% absorption depth) we interpret the derived values for  $\log N$  as lower limits (see the fifth column in Table 1).

#### 4.2. Component Modeling

A more advanced approach to derive column densities and gain more precise information on the velocity structure is the component modeling method. In this method, we model the shape of the metal absorption by considering multiple velocity components and take into account the instrumental line-spread function of the COS instrument (see Richter et al. 2013 for a detailed description of this method). Errors have been determined by varying  $N$  and  $b$  in the model in the allowed range, which is constrained by the residuals between the model spectrum and the data. All modeling results are presented in Table 2.

The weak absorption lines from O I  $\lambda 1302.2$  and Si II  $\lambda 1304.4$  can be successfully modeled with two relatively narrow absorption components at  $v_1 = +655$   $\text{km s}^{-1}$ , and  $v_2 = +720$ – $730$   $\text{km s}^{-1}$  and with Doppler parameters  $b_1 = 12$ – $15$   $\text{km s}^{-1}$ , and  $b_2 = 7$ – $10$   $\text{km s}^{-1}$ , hereafter referred to as comp. 1 and 2. The strong line of Si III  $\lambda 1206.5$  exhibits further a broad, absorption wing in the blue, extending down to  $\sim +500$   $\text{km s}^{-1}$  as well as moderate absorption near  $\sim +700$   $\text{km s}^{-1}$ , situated just between comp. 1 and 2. These features indicate the presence of additional absorption components for Si III (Figure 4).

The observed Si III absorption profile can be reproduced in our model by adding either one, very broad ( $b = 75$   $\text{km s}^{-1}$ ) absorption component centered at  $v = +660$   $\text{km s}^{-1}$  (Figure 4, middle panel) or by adding two moderately broadened satellite components to comp. 1 and 2 at  $v_3 = +625$   $\text{km s}^{-1}$  and  $v_4 = +710$   $\text{km s}^{-1}$  with  $b_3 = b_4 = 40$   $\text{km s}^{-1}$  (Figure 4, lower panel). The blue solid lines shown in the middle and lower panels of Figure 4, which display the resulting total absorption profile, do both reproduce the observed absorption profile of Si III very well.

The extremely high  $b$  value of  $75$   $\text{km s}^{-1}$ , which is required to match the profile with just one additional component, is unphysically high for a single, photo-ionized circumgalactic gas cloud, as neither thermal broadening nor large-scale turbulent gas motions are expected to boost the Doppler parameter to such high values (see, e.g., Herenz et al. 2013 for a statistics on  $b$  values in Milky Way CGM clouds). We

therefore reject this model, as it appears unrealistic. The second model with the two satellite components at  $+660$  and  $+710$   $\text{km s}^{-1}$  in Si III could be naturally explained by a core-envelope structure of the absorbing clouds, with comp. 3 and 4 being the outer ionized gas layers (envelopes) of comp. 1 and 2. Such multiphase absorbers are regularly seen in the local CGM and in circumgalactic Si II/Si III/Si IV systems around other low-redshift galaxies (Richter et al. 2016; Richter et al. 2017; Muzahid et al. 2018). While we cannot exclude that the velocity structure is even more complex than what is evident from the COS data, which are limited in spectral resolution and S/N, we here do not consider any other models with more than four absorption components. No valuable information would be gained from such hypothetical models. Note that the total Si III column density in the weak satellite components is constrained to  $\log N = 13.30 \pm 0.15$  and is independent of the actual number of absorption components. We will further discuss the multiphase nature of Spur 2 in Section 5.3.

From the modeling (Table 2), it follows that the ion column densities are relatively evenly distributed over the four absorption components. The total ion column densities (i.e., the sum over all four absorption components) are given in Table 1, sixth column. They are in good agreement with the total ion column densities derived from the AOD method (Table 1, fifth row).

#### 4.3. H I Ly $\alpha$ Absorption

The large velocity separation between the Galactic absorption and absorption from Spur2 around NGC 4631 allows us to model the H I Ly $\alpha$  absorption profile and obtain a precise estimate of the (pencil-beam) neutral gas column density in Spur 2 from the UV data. The H I Ly $\alpha$  absorption profile between  $-2000$  and  $+2000$   $\text{km s}^{-1}$  is shown in Figure 5, with the best-fitting model indicated with the red solid line. For the damped Milky Way disk absorption trough we assume a single absorption component centered at zero velocities with  $\log N$  (H I) = 19.78, predominantly constrained by the shape of the extended Lorentzian damping wing on the blue side of the absorption trough.

For the modeled Ly $\alpha$  absorption in Spur 2 in the range  $500$ – $1000$   $\text{km s}^{-1}$ , we assume two neutral absorption components fixed at the velocities of the two narrow O I components seen at  $v_1 = +655$   $\text{km s}^{-1}$  and  $v_2 = +720$   $\text{km s}^{-1}$  (Table 2).

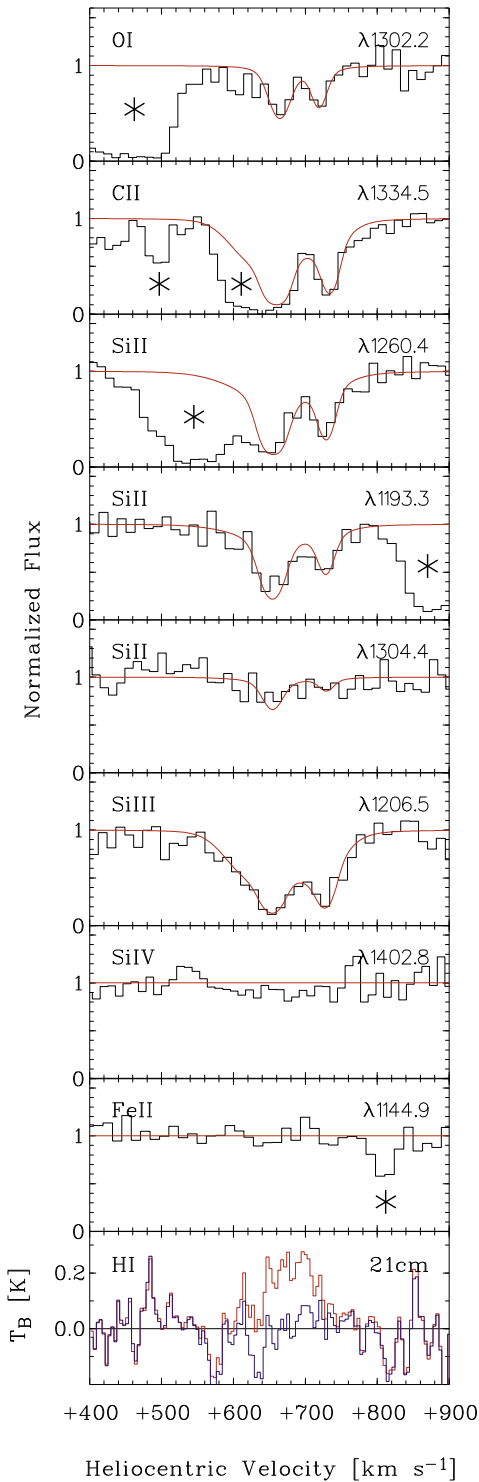


**Figure 3.** Absorption profiles of metal ions in the COS spectrum of 2MASS J12421031+3214268 and 21 cm emission profiles from the WSRT/GBT data. For displaying purposes, the COS data have been binned over 5 pixels. Absorption from Spur 2 around NGC 4631 is seen in the velocity range  $v_{\text{helio}} = +550$  to  $+800$  km s $^{-1}$ . The red solid line in the absorption spectra shows the best-fitting absorber model, as described in Section 4.2. The star symbols indicate blending lines not related to Spur 2. In the lowest panel (21 cm data), the blue and red solid lines indicate the emission spectra from the WSRT only and WSRT+GBT combined data set in the direction of 2MASS J12421031+3214268, respectively.

This approach is justified, because O I and H I have identical ionization potentials and they trace exactly the same gas phase. We further assume that the oxygen abundance in both

**Table 1**  
Summary of Column Density Measurements

Ion	$\lambda_0$ [Å]	$f^a$	$W_\lambda$ [mÅ]	$\log N_{\text{AOD}}^b$	$\log N_{\text{model}}^c$
O I	1302.17	0.048	$160 \pm 23$	$14.49 \pm 0.09$	$14.54 \pm 0.08$
C II <sup>d</sup>	1334.53	0.128	$162 - 412$	$\geq 14.11$	$14.93_{-0.53}^{+0.09}$
Si II	1193.29	0.582	$278 \pm 26$	$13.74 \pm 0.11$	$13.91 \pm 0.07$
	1260.42	1.176	$387 \pm 44$	$\geq 13.62$	$13.91 \pm 0.07$
	1304.37	0.086	$\leq 71$	$\leq 13.94$	$13.91 \pm 0.07$
Si III	1206.50	1.627	$488 \pm 32$	$\geq 13.61$	$13.79 \pm 0.12$
Si IV	1402.77	0.254	$\leq 67$	$\leq 13.28$	...
Fe II	1144.94	0.083	$\leq 36$	$\leq 13.79$	...

**Notes.**

<sup>a</sup> Oscillator strength (Morton 2003).

<sup>b</sup> Total column density in Spur 2, obtained by integrating the ion profiles in the range  $v_{\text{helio}} = 550\text{--}800$  km s $^{-1}$ .

<sup>c</sup> Total column density in Spur 2, obtained by summing over  $N$  in all velocity components based on the component model described in Section 4.2.

<sup>d</sup> C II is blended by intervening H I Ly  $\zeta$  absorption at  $z = 0.043677$ .

narrow components is identical, so that

$$\frac{N_1(\text{O I})}{N_2(\text{O I})} = \frac{N_1(\text{H I})}{N_2(\text{H I})}. \quad (1)$$

This approach allows us to fix the column density ratio in the H I Ly $\alpha$  model to that of O I and thus only the total H I column density remains as a free parameter in the model, if a constant metallicity is assumed. Doing this, the total H I column density in Spur 2 toward 2MASS J12421031+3214268 comes out to  $\log N(\text{H I}) = 18.68 \pm 0.15$ . As can be seen in Figure 5, the resulting model reproduces the observed shape of the observed Ly $\alpha$  absorption very well.

There is no evidence that comp. 3 and 4 seen in Si III contribute significantly to the H I Ly $\alpha$  absorption. This is in line with the idea that they contain predominantly *ionized* gas with a small neutral gas fraction.

#### 4.4. 21 cm Emission

Figure 1 indicates that the QSO sightline passes the tidal streams around NGC 4631 just beyond the outer boundaries of the 21 cm intensity contours of Spur 2. The H I column density measured from the Ly $\alpha$  absorption ( $\log N(\text{H I}) = 18.68$ ; see above) is below the detection limit of the high-resolution HALOGAS/WSRT data, suggesting that the 2MASS J12421031+3214268 sightline traces the diffuse outer envelope of Spur 2. In the lowest panel of Figure 3, we show the 21 cm emission spectrum in the range  $v_{\text{helio}} = 400\text{--}900$  km s $^{-1}$  from the HALOGAS/WSRT data cube centered on the position of 2MASS J12421031+3214268 (blue solid line). No significant emission is seen in the WSRT data (as expected), but we can place an upper limit on the H I column density of  $\log N(\text{H I}) = 19.15$ . This is in line with the measured value of  $\log N(\text{H I}) = 18.68$  from the Ly $\alpha$  absorption. With the red solid line we have overlaid the 21 cm emission spectrum from the *combined* WSRT+GBT data, which has a substantially larger effective beam size at the position of the QSO (see discussion in Section 3.2). A weak ( $T_{\text{B,max}} \approx 0.25$  K) emission peak is seen at  $+680$  km s $^{-1}$ , corresponding to  $\log N(\text{H I}) = 19.65$ . This feature is a result of beam-smearing effects near the 21 cm boundary of Spur 2, caused by the low angular resolution of the combined WSRT+GBT data. A substantial fraction of the combined WSRT+GBT beam centered on 2MASS J12421031+3214268 is filled with

**Table 2**  
Parameters for the Absorption-line Modeling

Ion	$v_1$ (km s <sup>-1</sup> )	$b_1$ (km s <sup>-1</sup> )	$\log N_1$	$v_2$ (km s <sup>-1</sup> )	$b_2$ (km s <sup>-1</sup> )	$\log N_2$	$v_3$ (km s <sup>-1</sup> )	$b_3$ (km s <sup>-1</sup> )	$\log N_3$	$v_4$ (km s <sup>-1</sup> )	$b_4$ (km s <sup>-1</sup> )	$\log N_4$
O I	+665	12	14.35	+720	7	14.10	+625	...	...	+710	...	...
C II	+655	15	14.70 <sup>a</sup>	+730	10	14.20	+625	40	14.00 <sup>a</sup>	+710	40	13.80
Si II	+655	15	13.60	+730	10	13.10	+625	40	≤13.40	+710	40	≤13.10
Si III	+655	15	13.35	+730	10	13.30	+625	40	13.00	+710	40	13.00
H I	+655	25	18.50	+730	20	18.25	+625	...	...	+710	...	...

**Note.**

<sup>a</sup> Comp. 1 blended by intervening H I Ly  $\zeta$  absorption at  $z = 0.043677$ .

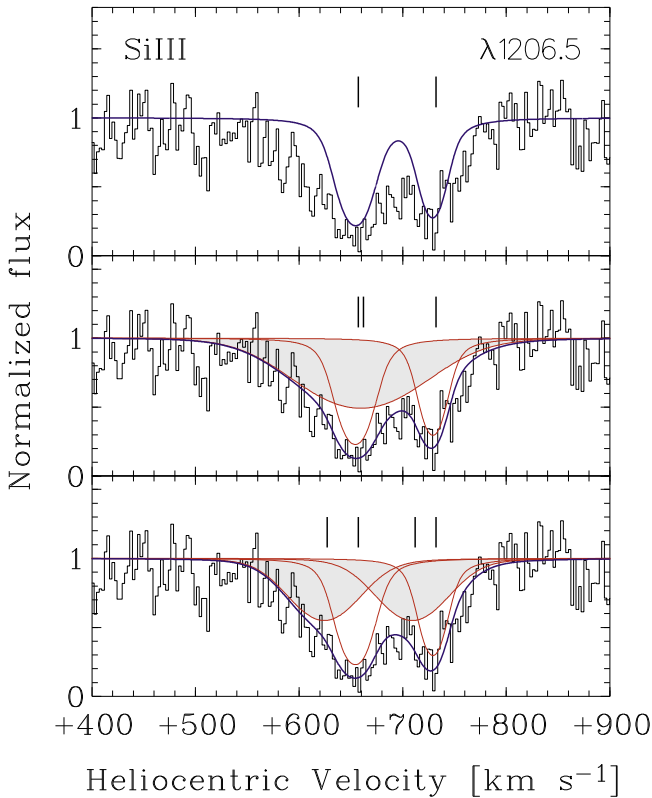


**Figure 4.** Decomposition of absorption profiles in the COS data, here demonstrated for the strong Si III  $\lambda 1206.5$  line. Next to the two narrow components 1 and 2 (upper panel) a third, very broad satellite component (middle panel) or, alternatively, two additional, moderately broadened satellite components (lower panel) are required in the component model to match the data (see Section 4.2 for details).

21 cm emission from the inner region of Spur 2, leading to the observed emission feature.

## 5. Discussion

### 5.1. Metallicity of the Gas

Because of the identical ionization potentials of neutral oxygen and hydrogen and the unimportance of dust depletion effects for O, the O I/H I ratio is a reliable indicator for the overall  $\alpha$  abundance in neutral gas. For  $\log N(\text{H I}) > 18$ , only very small ionization corrections ( $< 0.1$  dex) apply (see, e.g., Richter et al. 2018).

From the O I and H I column densities listed in Table 2 and and the ionization model described in Section 5.3, we determine a metallicity of the gas of  $0.13^{+0.07}_{-0.05}$  solar or  $[\alpha/\text{H}] = -0.90 \pm 0.16$ , where we assume a solar oxygen reference

abundance of  $(\text{O}/\text{H})_{\odot} = -3.31 \pm 0.05$  (Asplund et al. 2009). Such a metallicity is at the low end of the  $\alpha$ -abundance distribution observed in massive spiral galaxies (Pilyugin et al. 2014), but is very similar to the values found in the main body of the Magellanic Stream (MS) and other HVCs in the halo of the Milky Way (Richter et al. 2001; Tripp et al. 2003; Fox et al. 2013).

Interestingly, the derived metallicity of  $[\alpha/\text{H}] = -0.90 \pm 0.16$  in Spur 2 falls right into the metallicity gap seen in LLS at low redshifts (Lehner et al. 2013 their Figure 3). In terms of metallicity, Spur 2 around NGC 4631 and the MW HVCs thus appear to be atypical for optically thick H I absorbers in the local universe. It remains to be explored in future studies whether this is due to the limited statistics on the metallicity of low-redshift LLS or could be related to the tidal origin of Spur 2, the MS, and other MW HVCs.

### 5.2. Possible Sources of Spur 2

In the following, we discuss the various possible sources of Spur 2 by combining our metallicity measurement with other available information.

#### 5.2.1. The Outer Disk of NGC 4631

One possible scenario is that Spur 2 represents gas that has been tidally torn out of the outer, metal-poor gas disk of NGC 4631 during a close encounter of NGC 4627 or another satellite galaxy. Spur 2 does appear to connect spatially and kinematically with the outer NGC 4631 H I disk over a large section of the disk's major axis (Rand 1994), which supports an NGC 4631 disk origin.

The derived metallicity of  $[\alpha/\text{H}] = -0.90 \pm 0.16$  in Spur 2 is, however, significantly below the interstellar oxygen abundance in the central region of the NGC 4631 disk ( $[\text{M}/\text{H}] = -0.30 \pm 0.06$ ; Pilyugin et al. 2014). If we apply the observed radial metallicity gradient for NGC 4631 of  $-0.0194 \pm 0.0073$  dex/kpc (Pilyugin et al. 2014), the derived  $\alpha$  abundance in Spur 2 would match the metallicity of NGC 4631 only in the very outer disk at  $r > 20$  kpc. Most likely, the extrapolation to such large radii is not valid, as the metallicity gradients in disk galaxies appear to flatten out at large radii (Werk et al. 2011). Therefore, the measured low  $\alpha$  abundance in Spur 2 does not favor an origin in the disk of NGC 4631.

We further note that the initial metallicity of Spur 2, at the time when the gas was separated from its source galaxy, could have been even lower than what is observed today. This is because the tidal features potentially have started to mix with the ambient hot coronal gas around NGC 4631, which is expected to be fed by outflowing, chemically enriched material

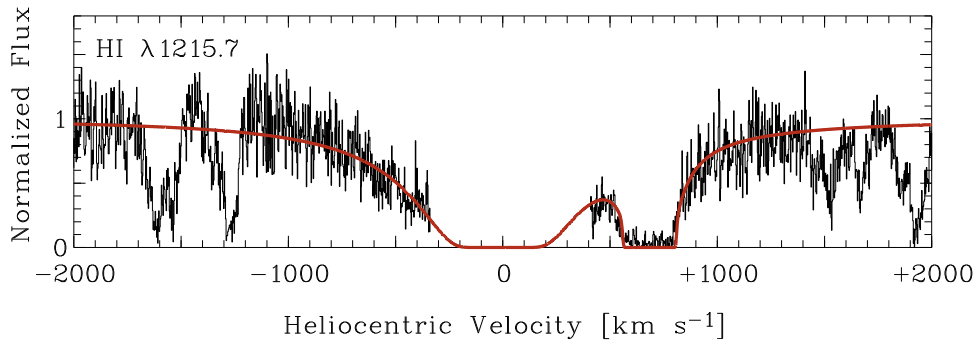


**Figure 5.** Modeling of the HI Ly $\alpha$  absorption in the COS spectrum of 2MASS J12421031+3214268. The red solid line shows the best-fitting model with Ly $\alpha$  absorption from the Milky Way disk and halo gas near zero velocities and Ly $\alpha$  absorption from the NGC 4631 stream near +700 km $^{-1}$  (see Section 4.3).

from star-forming regions and thus should be more metal-rich (see review by Fraternali 2017).

### 5.2.2. NGC 4627 or other Satellite Galaxies

Alternatively, Spur 2 could represent material that has been stripped from a gas-rich companion of NGC 4631. The stripped gas would then be located in the halo of NGC 4631 and currently being accreted onto the disk, which would explain its spatial and kinematical connection to the HI disk. Possible galaxy candidates are the dE satellite NGC 4627, or the tidally disrupted satellite galaxy that forms the recently detected stellar stream around NGC 4631 (Martínez-Delgado et al. 2015), or another recently disrupted gas-rich satellite galaxy.

Combes (1978) has presented a detailed model of the tidal interactions between NGC 4631, NGC 4656, and NGC 4627 based on the early 21 cm observations presented in Welichew et al. (1978). From her model, which assumes a parabolic encounter of NGC 4656 with NGC 4631, follows that basically all gaseous material that is seen in Spurs 1, 4, and 5 and in the gas near NGC 4656 stems from the NGC 4631 disk. Spurs 2 and 3, however, cannot be explained with this model. Combes proposes that the gas-rich progenitor galaxy of NGC 4627 has lost basically all its interstellar neutral gas in a close encounter with NGC 4631, material that is now seen in 21 cm emission as Spurs 2 and 3. While the Combes model disfavors the nearby companion NGC 4656 as source for Spur 2, it is worth noticing that the measured  $\alpha$  abundance in Spur 2 coincides well with the interstellar metallicity in the inner 10 kpc of NGC 4656 (Pilyugin et al. 2014). If some of the neutral material in the gaseous bridge between NGC 4631 and NGC 4656 is connected to the extended HI halo of NGC 4656, then it cannot be excluded that the absorption toward MASS J12421031+3214268 is related to gas that originally stems from NGC 4656. Clearly, it would be highly desirable to remodel the tidal interactions between NGC 4631, NGC 4656, and NGC 4627 using state-of-the-art simulation codes together with the most recent observational constraints as input parameters to further clarify these issues.

It is an interesting fact that the derived oxygen abundance of  $[M/H] = -0.90$  in Spur 2 matches almost exactly the metallicity derived for the stellar stream ( $[M/H] = -0.92$ ; Tanaka et al. 2017). The uncertainty for the stellar abundance is quite large, however, with a 90% confidence interval between  $-1.46$  and  $-0.51$  (see Tanaka et al. 2017). Therefore, this apparent similarity does not provide strong constraints on a possible common origin. There are, in fact, several arguments that speak against a connection between the stellar and the

gaseous streams. From the tidal model of Martínez-Delgado et al. (2015) it follows, for instance, that the stellar stream must be old, with a preferred age of  $\sim 3.5$  Gyr to qualitatively match the observed morphology of the stream. Spur 2 must be substantially younger, however, because the stream’s gas is expected to interact with the ambient hot coronal gas (e.g., Heitsch & Putman 2009). As a result, the gas should either be disrupted and incorporated into the corona, or be accreted onto the disk of NGC 4631 on timescales much smaller than 3.5 Gyr (typical disruption timescales would be a few 100 Myr; Heitsch & Putman 2009), i.e., the gas structure would not survive for such a long time in such a massive galaxy halo. Another result of the tidal model from Martínez-Delgado et al. (2015) is that the total initial stellar mass of the accreted dwarf galaxy must have been small,  $< 6 \times 10^8 M_{\odot}$ . This value is, however, smaller than the neutral gas mass of Spur 2 alone ( $\sim 8 \times 10^8 M_{\odot}$ ; Rand 1994). In conclusion, Spur 2 is almost certainly not related to the stellar stream.

### 5.3. Ionization Conditions and Total Gas Mass

We now discuss the ionization conditions in the different gas components in more detail by analyzing the observed O I/C II/Si II column density ratios with a grid of Cloudy ionization models (Ferland et al. 2013) that are based on the HI column densities (limits) derived for comp. 1 and 2 (Table 2).

We follow the strategy outlined in our previous studies (e.g., Richter et al. 2009, 2013, 2016, 2018) and model the ionization conditions in Spur 2 assuming the absorbers to be a simple gas slab that is illuminated from both sides. In principle, the strength and shape of the illuminating radiation field in a CGM cloud of a star-forming galaxy depends on the overall extragalactic UV background field at that redshift and the location of the cloud with respect to the UV-emitting star-forming disk. Since we are lacking any accurate information on the distance of Spur 2 to the NGC 4631 stellar disk and the shape/intensity of the local radiation field, we consider three models with different assumptions for the local radiation field in Spur 2. In the first model, we use only the extragalactic UV background (UVB) field at  $z = 0$  normalized to a photoionization rate of  $\log \Gamma = -13.34$  (see the discussion in Kollmeier et al. 2014; Shull et al. 2015; Wakker et al. 2015). The second model assumes a standard UVB field together with an additional Milky Way-type radiation field (Fox et al. 2005, 2014) at a galactocentric distance of  $d = 50$  kpc (UVB+G50), as explained in Fox et al. (2014) and Richter et al. (2009). The third model assumes a UVB field with an additional Milky



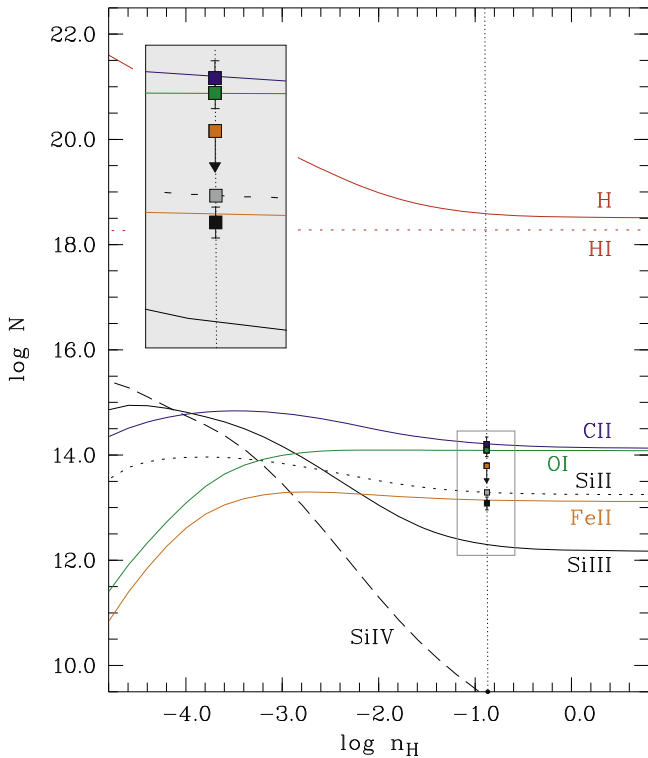


**Figure 6.** Predicted column densities (solid lines) for various ions as a function of the gas density from the Cloudy ionization model for comp. 2, assuming just the UV background as the ionization source (see Section 5.3; Table 3). The observed values (filled boxes) fit best to a gas density of  $\log n_{\text{H}} = -0.87$ . The gray box symbol indicates the Si II column density assuming a depletion of  $\log \delta(\text{Si}) = -0.22$  dex. The gray-shaded inset displays a zoom-in of the region indicated with the gray solid frame.

Way-type radiation field at a galactocentric distance of  $d = 10$  kpc (UVB+G10).

For the HI column densities in components 1 and 2, the expected ionization correction to determine (O/H) from the measured O I/H I is only 0.03 dex. For the derived  $\alpha$  abundance in the gas ( $[\alpha/\text{H}] = -0.90$ ), Cloudy then delivers for each of the three assumed radiation fields (UVB, UVB+G50, UVB+G10) predictions for the column densities of the other ions as a function of the local gas density,  $\log n_{\text{H}}$  (see Figure 6 for a Cloudy example plot). By matching the observed column densities with the Cloudy model predictions for UVB, UVB+G50, and UVB+G10, we obtain for each component an estimate for the ionized gas column density,  $N(\text{H II})$ , the gas density, the neutral gas fraction,  $f_{\text{HI}} = N(\text{H I})/[N(\text{H I}) + N(\text{H II})]$ , and the thickness of the absorbing gas layer,  $l = N(\text{H})/n_{\text{H}}$ . The modeling results are listed in Table 3.

Note that we do not include Si III in our modeling for comp. 1 and 2, as Si III and O I/Si II are not expected to arise in the same gas phase (see discussions in Richter et al. 2016; Muzahid et al. 2018). The fine-tuning of the Si II/O I ratio in comp. 1 and 2 in the Cloudy models was used to determine the dust depletion of Si, as will be described in Section 5.4.

From the Cloudy modeling, it follows that the density in comp. 1 lies between  $\log n_{\text{H}} = -2.18$  and  $-0.64$ , which indicates an absorber size between  $\sim 30$  pc and 1 kpc, depending on the assumed radiation field (see Table 3). The gas density in comp. 2 is predicted to be one order of magnitude higher ( $\log n_{\text{H}} = -0.87$  to  $+0.67$ ), indicating that comp. 2 represents a small gas clump with a size  $\leq 10$  pc. It is

important to keep in mind that these values are based on the above outlined (idealized) assumptions on the radiation field and absorber geometry. Consequently, they should be interpreted with some caution. If Spur 2 has a similarly large distance to the disk of NGC 4631 as the main body of the MS to the MW disk ( $d = 50$ – $100$  kpc), then the UVB+G50 model applies, indicating that the absorbing clouds have parsec-scale sizes at moderate densities. In this model, which we regard as the most realistic one given the geometrical configuration of the Spurs around NGC 4631, the derived gas densities and clump sizes are very similar to those seen in the MS and other HVCs in the Milky Way halo (Richter et al. 2009, 2013, 2018), pointing at comparable physical conditions.

While we cannot provide any Cloudy modeling for the satellite components 3 and 4, we can give a lower limit for the total hydrogen column density,  $N(\text{H}) = N(\text{H I}) + N(\text{H II})$ , in each of these components. For this, we transform the observed Si III column density in comp. 3 and 4 (Table 2) into  $N(\text{H})$  assuming that the silicon abundance in the gas is 0.13 solar, similar to what is measured in comp. 1 and 2. With the resulting value  $\log(\text{Si}/\text{H}) = -5.29$  in Spur 2, we find that  $\log N(\text{H}) \geq 18.29$  in each of the two comp. 3 and 4, or  $\log N(\text{H}) \geq 18.59$  in the two components together.

Combining the results for all four components, we derive for the mean neutral gas fraction in Spur 2 along the 2MASS J12421031+3214268 sightline a value of  $\langle f_{\text{HI}} \rangle = 0.14$ , indicating that there is  $\sim 7$  times more ionized hydrogen than neutral hydrogen in the stream in this direction. This ratio may not be typical for the entire tidal stream. This is because the 2MASS J12421031+3214268 sightline passes the stream just at the boundaries of the 21 cm contours where the neutral gas column is substantially smaller than in the inner regions of Spur 2 (see Figure 1, upper panel). Yet, the Cloudy results imply that Spur 2 contains substantial amounts of ionized gas that most likely brings its total gas mass to a few times  $10^9 M_{\odot}$ . This value is comparable to the total gas mass estimated for the Magellanic Stream in the Milky Way halo (Fox et al. 2014).

#### 5.4. Dust Content

As has been demonstrated in the case of the Magellanic Stream, interstellar dust grains can survive the tidal stripping process in merging galaxies (Lu et al. 1998; Gibson et al. 2001; Fox et al. 2013; Richter et al. 2013, 2018). To investigate the dust abundance in Spur 2, we compare in detail the abundance of the two  $\alpha$  elements Si and O in our Cloudy model for components 1 and 2. The Si/O abundance ratio is a useful dust indicator. This is because even in relatively diffuse gas in the Milky Way’s ISM and CGM, Si is moderately depleted into dust grains, while O is not (e.g., Savage & Sembach 1996).

The Cloudy models for comp. 1 and 2 predict Si II column densities that are systematically higher than those observed, suggesting that Si indeed is depleted into dust grains. The effect is small, however, with an absolute depletion value of only  $|\log \delta(\text{Si})| = 0.22$  dex (Table 3, fourth row). This value corresponds roughly to the systematic errors in the Cloudy model, so in the following we regard  $|\log \delta(\text{Si})| \leq 0.2$  dex as a realistic upper limit for the Si depletion in Spur 2.

Interestingly, this upper limit is still substantially smaller than the characteristic Si depletion values recently observed in the Magellanic Stream, its Leading Arm, and the Magellanic Bridge ( $|\log \delta(\text{Si})| \geq 0.5$  dex; Lehner 2002; Fox et al. 2013;

**Table 3**  
Results from Ionization Models

Comp.	$v$ [km s <sup>-1</sup> ]	log $N(\text{H I})$	log $\delta(\text{Si})$ [dex]	UV model	log $N(\text{H II})$	log $n_{\text{H}}$	log $f_{\text{HI}}$	$l$ [pc]
1	+655	18.45	-0.22	UVB	19.25	-2.18	-0.86	1000
				UVB+G50	19.25	-1.40	-0.86	166
				UVB+G10	19.25	-0.64	-0.86	29
2	+730	18.30	-0.22	UVB	18.55	-0.87	-0.53	10
				UVB+G50	18.55	-0.09	-0.53	2
				UVB+G10	18.55	+0.67	-0.53	0.3

**Notes.**

<sup>a</sup> Only the gas phase traced by O I, C II, and Si II is considered.

<sup>b</sup> Si depletion value.

<sup>c</sup> UV flux models considered: (1) EG = extragalactic UV background at  $z = 0$ ; (2) EG+G50kpc = extragalactic UV background + galaxy contribution assuming  $d = 50$  kpc impact parameter; (3) EG+G10kpc = EG+galaxy at  $d = 10$  kpc.

Richter et al. 2013, 2018). As discussed in Richter et al. (2018), the level of depletion in star-less tidal streams possibly reflect the initial conditions in the interstellar medium of the stream’s source galaxy, if the gas has been removed “quiescently” from its host (e.g., by gravitational forces), but not by dust-destroying energetic events (e.g., by stellar winds or supernova-driven outflows). Therefore, independently of whether Spur 2 originally stems from a satellite galaxy or from the outer disk of NGC 4631, the small absolute Si depletion value in Spur 2 indicates an overall low dust content in the original host environment of the gas.

## 6. Summary and Conclusions

We have analyzed *HST*/COS UV spectral data of the background QSO 2MASS J12421031+3214268 and 21 cm observations from the HALOGAS project with support from new GBT observations to study the chemical composition and physical conditions in one of the tidal gas streams (Spur 2) around the Whale galaxy NGC 4631. The main results of our study can be summarized as follows:

1. Strong metal and hydrogen absorption related to Spur 2 is detected in the COS spectrum of 2MASS J12421031+3214268 in the velocity range between +550 and 800 km s<sup>-1</sup>, although the sightline passes the stream just beyond the outer 21 cm boundaries. Detected atoms/ions include H I, O I, C II, Si II, and Si III.
2. Four individual velocity components are identified in the metal absorption with two narrow components ( $b = 7\text{--}15$  km s<sup>-1</sup>) and two broader components ( $b = 40$  km s<sup>-1</sup>). The broader components, which are seen only in Si III, possibly trace more extended, ionized gas layers that surround the denser gas structures sampled by the low-ionization states. This complex absorption pattern suggests a multiphase nature of the tidal gas stream, similar to what is seen in the Magellanic Stream in the outer Milky Way halo.
3. A fit to the H I Ly $\alpha$  absorption in the 2MASS J12421031+3214268 spectrum yields a neutral gas column density of  $\log N(\text{H I}) = 18.68 \pm 0.15$  in Spur 2, which is below the detection limit in the 21 cm data. From a set of Cloudy ionization models, it follows that the total hydrogen column in Spur 2 toward 2MASS J12421031+3214268 is  $\log N(\text{H}) = 19.46$ , indicating a sightline-averaged neutral gas fraction of 14%. The gas density in the narrow absorption components range between log

$n_{\text{H}} = -2.18$  to  $+0.67$ , suggesting that these absorbers are CGM cloudlets on subkiloparsec scales.

4. From the unsaturated O I absorption, together with the derived H I column density and the Cloudy ionization correction, we derive an  $\alpha$  abundance in the gas of  $(\alpha/\text{H}) = 0.13_{-0.04}^{+0.05}$  solar ( $[\alpha/\text{H}] = -0.90 \pm 0.16$ ). This value is lower than the abundance in the NGC 4631 gas disk, even if the radial abundance gradient is taken into account. Although the kinematic connection of Spur 2 with the gas disk (Rand 1994) points toward an NGC 4631 disk origin, the low metallicity in the gas rather favors a satellite-galaxy origin for Spur 2. From the Cloudy models, we derive an upper limit for the Si depletion in Spur 2 of  $|\log \delta(\text{Si})| \leq 0.2$ , suggesting that the gas has a low dust abundance.

We conclude that the observed properties of Spur 2 favor the scenario, in which metal- and dust-poor gas has been tidally torn out of a (formerly) gas-rich satellite galaxy in a recent encounter. The dE satellite NGC 4627 at 6 kpc distance from NGC 4631 thus represents a particularly promising candidate for the encountering galaxy.

The ionization conditions in the gas observed toward 2MASS J12421031+3214268 further indicate that Spur 2 contains  $\sim 7$  times more ionized than neutral gas, which lifts its total mass to a value of a few times  $10^9 M_{\odot}$ . If similar ionization fractions apply to the other spurs around NGC 4631, however, then the combined total gas mass of the NGC 4631 tidal gas streams may easily exceed  $10^{10} M_{\odot}$ . This extremely large reservoir of relatively cool ( $T < T_{\text{vir}}$ ), metal-poor circumgalactic gas will potentially be accreted by NGC 4631 over the next few hundred megayears and will boost its star formation rate. Additional information on the chemical composition and physical conditions of the other four spurs of the Whale galaxy’s tidal stream system would require a larger number of UV-bright background AGNs distributed around NGC 4631, which unfortunately are not available. From what we know so far, however, the NGC 4631 gas spurs reflect many of the properties seen in the the Magellanic Stream and its various components (Mathewson et al. 1974; Putman et al. 1998; Brüns et al. 2005; D’Onghia & Fox 2016).

While the analysis of individual QSO sightlines around nearby galaxy mergers provide interesting information on these particular systems, a more systematic approach in studying the neutral and ionized gas distribution in group environments is highly desirable. As demonstrated here, absorption spectroscopy

in the UV represents a powerful method to characterize the multiphase nature of tidal gas streams, to estimate their chemical composition, and their ionized gas mass along individual sightlines. The combination of a larger sample of QSO sightlines passing nearby galaxy groups, data from future deep 21 cm surveys, deep X-ray observations, and high-resolution hydrodynamical simulations holds the prospect of substantially improving our understanding of the overall importance of massive tidal gas streams in the context of galaxy formation.

This work is based on observations obtained under program 14085 with the NASA/ESA *Hubble Space Telescope*, which is operated by the Space Telescope Science Institute (STScI) for the Association of Universities for Research in Astronomy, Inc., under NASA contract NAS5D26555.

## Appendix

### Combination of WSRT and GBT Data

The CASA task “feather,” which was used to combine the GBT with the WSRT data, first regrids the GBT data to match the spectral and spatial resolution of the WSRT data before Fourier transforming each image to a gridded  $u-v$  plane. The  $u-v$  data of the GBT are then scaled by the ratio of the volume of the two beams

$$\alpha = \frac{\Omega_{\text{WSRT}}}{\Omega_{\text{GBT}}}, \quad (2)$$


where we find  $\alpha$  to equal 0.0059. This factor accounts for the difference in flux of the two data sets based solely on the differences in resolution. The WSRT  $u-v$  data are then scaled by the factor

$$\beta = 1 - \mathfrak{F}[B_{\text{GBT}}], \quad (3)$$

where the second term represents the Fourier transform of the GBT beam as a function of sky angles. The two scaled  $u-v$  data sets are then summed and Fourier transformed back to the image plane. The scaling depicted in Equation (3) ensures that the effects of the poorly sampled low spatial frequencies in the WSRT data are smoothly removed before the well-sampled low spatial frequencies provided by the GBT data are added.

Before computing the zeroth (top) and first (bottom) statistical moments of the cube as shown in Figure 1, the combined cube was masked at the  $3\sigma_K$  ( $\sigma = 10$  mK) level to ensure only emission is included in the final maps. Additionally, an unmasked spectrum was extracted at the position of the QSO sightline, which yields an upper column density limit of  $\log N(\text{HI}) = 19.53$ .

## ORCID iDs

P. Richter  <https://orcid.org/0000-0002-1188-1435>  
 B. Winkel  <https://orcid.org/0000-0001-6999-3635>  
 B. P. Wakker  <https://orcid.org/0000-0002-0507-7096>  
 A. J. Fox  <https://orcid.org/0000-0003-0724-4115>  
 R. A. M. Walterbos  <https://orcid.org/0000-0002-0782-3064>  
 L. Zschaechner  <https://orcid.org/0000-0002-9919-8672>

## References

Ann, H. B., Seo, M. S., & Baek, S.-J. 2011, *JKAS*, 44, 23  
 Asplund, M., Grevesse, N., Jacques Sauval, A., & Scott, P. 2009, *ARA&A*, 47, 481  
 Barger, K. A., Haffner, L. M., & Bland-Hawthorn, J. 2013, *ApJ*, 771, 132

Bendo, G. J., Dale, D. A., Draine, B. T., et al. 2006, *ApJ*, 652, 283  
 Besla, G., Kallivayalil, N., Hernquist, L., et al. 2010, *ApJL*, 721, L97  
 Besla, G., Kallivayalil, N., Hernquist, L., et al. 2012, *MNRAS*, 421, 2109  
 Brüns, C., Kerp, J., Staveley Smith, L., et al. 2005, *A&A*, 432, 45  
 Chynoweth, K. M., Langston, G. I., Yun, M. S., et al. 2008, *AJ*, 135, 1983  
 Combes, F. 1978, *A&A*, 65, 47  
 Connors, T. W., Kawata, D., & Gibson, B. K. 2006, *MNRAS*, 371, 108  
 D’Onghia, E., & Fox, A. J. 2016, *ARA&A*, 54, 363  
 Daveé, R., Finlator, K., & Oppenheimer, B. D. 2012, *MNRAS*, 421, 98  
 Debes, J. H., Becker, G., Roman-Duval, J., et al. 2016, Instrument Science Report COS 15, [http://www.stsci.edu/hst/cos/documents/isrs/ISR2016\\_15.pdf](http://www.stsci.edu/hst/cos/documents/isrs/ISR2016_15.pdf)  
 Di Teodoro, E. M., & Fraternali, F. 2014, *A&A*, 567, 68  
 Diaz, J. D., & Bekki, K. 2011, *MNRAS*, 413, 2015  
 Diaz, J. D., & Bekki, K. 2012, *ApJ*, 750, 36  
 Fabbiano, G., & Trinchieri, G. 1987, *ApJ*, 315, 46  
 Ferland, G. J., Porter, R. L., van Hoof, P. A. M., et al. 2013, *RMxAA*, 49, 137  
 Finlator, K. 2017, *ASSL*, 430, 221  
 Fontana, A., & Ballester, P. 1995, *Msngr*, 80, 37  
 Fox, A. J., Barger, K. A., Wakker, B. P., et al. 2018, *ApJ*, 854, 142  
 Fox, A. J., Richter, P., Wakker, B. P., et al. 2013, *ApJ*, 772, 110  
 Fox, A. J., Wakker, B. P., Barger, K. A., et al. 2014, *ApJ*, 787, 147  
 Fox, A. J., Wakker, B. P., Savage, B. D., et al. 2005, *ApJ*, 630, 332  
 Fraternali, F. 2017, *ASSL*, 430, 323  
 Fraternali, F., & Binney, J. J. 2008, *MNRAS*, 386, 935  
 Gardiner, L. T., & Noguchi, M. 1996, *MNRAS*, 278, 191  
 Gentile, G., Józsa, G. I. G., Serra, P., et al. 2013, *A&A*, 554, A125  
 Gibson, B. K., Giroux, M. L., Penton, S. V., et al. 2001, *AJ*, 122, 3280  
 Giuricin, G., Marinoni, C., Ceriani, L., & Pisani, A. 2000, *ApJ*, 543, 178  
 Green, J. C., Froning, C. S., Osterman, S., et al. 2012, *ApJ*, 744, 60  
 Heald, G., Józsa, G., Serra, P., et al. 2011, *A&A*, 526, A118  
 Heitsch, F., & Putman, M. E. 2009, *ApJ*, 698, 1485  
 Herenz, P., Richter, P., Charlton, J. C., & Masiero, J. R. 2013, *A&A*, 550, A87  
 Kacprzak, G. 2017, *ASSL*, 430, 145  
 Kamphuis, P., Rand, R. J., Józsa, G. I. G., et al. 2013, *MNRAS*, 434, 2069  
 Kennicutt, R. C., Lee, J. C., Funes, S. J., et al. 2008, *ApJS*, 178, 247  
 Kollmeier, J. A., Weinberg, D. H., Oppenheimer, B. D., et al. 2014, *ApJL*, 789, L32  
 Lehner, N. 2002, *ApJ*, 578, 126  
 Lehner, N., Howk, J. C., Tripp, T. M., et al. 2013, *ApJ*, 770, 138  
 Lu, L., Sargent, W. L. W., Savage, B. D., et al. 1998, *AJ*, 115, 162  
 Martin, C., & Kern, B. 2001, *ApJ*, 555, 258  
 Martínez-Delgado, D., D’Onghia, E., Chonis, T. S., et al. 2015, *AJ*, 150, 116  
 Mathewson, D. S., Cleary, M. N., & Murray, J. D. 1974, *ApJ*, 190, 291  
 Melo, V., & Muñoz-Tuñón, C. 2002, in ASP Conf. Ser. 282, *Galaxies: The Third Dimension*, ed. M. Rosada, L. Binette, & L. Arias (San Francisco, CA: ASP), 338  
 Morton, D. C. 2003, *ApJS*, 149, 205  
 Muzahid, S., Fonseca, G., Roberts, A., et al. 2018, *MNRAS*, 476, 4965  
 Neinger, N., & Dumke, M. 1999, *PNAS*, 96, 5360  
 Nidever, D. L., Majewski, S. R., Burton, W. B., & Nigra, L. 2010, *ApJ*, 723, 1618  
 Pilyugin, L. S., Grebel, E. K., & Kniazev, A. Y. 2014, *AJ*, 147, 131  
 Pingel, N. M., Pisano, D. J., Heald, G., et al. 2018, *ApJ*, 865, 36  
 Pisano, D. J. 2014, *AJ*, 147, 48  
 Putman, M. E., Gibson, B. K., Staveley-Smith, L., et al. 1998, *Natur*, 394, 752  
 Radburn-Smith, D. J., de Jong, R. S., Seth, A. C., et al. 2011, *ApJS*, 195, 18  
 Rand, R. 1994, *A&A*, 285, 833  
 Richter, P. 2017, *ASSL*, 430, 15  
 Richter, P., Charlton, J. C., Fangano, A. P. M., Ben Bekhti, N., & Masiero, J. R. 2009, *ApJ*, 695, 1631  
 Richter, P., Fox, A. J., Wakker, B. P., et al. 2013, *ApJ*, 772, 111  
 Richter, P., Fox, A. J., Wakker, B. P., et al. 2018, *ApJ*, 865, 145  
 Richter, P., Nuza, S. E., Fox, A. J., et al. 2017, *A&A*, 607, A48  
 Richter, P., Savage, B. D., Wakker, B. P., Sembach, K. R., & Kalberla, P. M. W. 2001, *ApJ*, 549, 281  
 Richter, P., Wakker, B. P., Fechner, C., et al. 2016, *A&A*, 590, A68  
 Roberts, M. S. 1968, *ApJ*, 151, 117  
 Salem, M., Besla, G., Bryan, G., et al. 2015, *ApJ*, 815, 77  
 Sánchez-Almeida, J. 2017, *ASSL*, 430, 67  
 Sanders, D. B., Mazzarella, J. M., Kim, D.-C., Surace, J. A., & Soifer, B. T. 2003, *AJ*, 126, 1607

- Savage, B. D., & Sembach, K. R. 1991, [ApJ](#), **379**, 245
- Savage, B. D., & Sembach, K. R. 1996, [ARA&A](#), **34**, 279
- Shull, J. M., Moloney, J., Danforth, C. W., & Tilton, E. M. 2015, [ApJ](#), **811**, 3
- Tanaka, M., Chiba, M., & Komiyama, Y. 2017, [ApJ](#), **842**, 127
- Tripp, T. M., Wakker, B. P., Jenkins, E. B., et al. 2003, [AJ](#), **125**, 3122
- Wakker, B. P., Hernandez, A. K., French, D., et al. 2015, [ApJ](#), **814**, 40
- Wang, Q. D., Walterbos, R. A. M., Steakley, M. F., Norman, C. A., & Braun, R. 1995, [ApJ](#), **439**, 176
- Weliachew, L., Sancisi, R., & Guélin, M. 1978, [A&A](#), **65**, 37
- Werk, J. K., Putman, M. E., Meurer, G. R., & Santiago-Figueroa, N. 2011, [ApJ](#), **735**, 71
- Yamasaki, N. Y., Sato, K., Mitsuishi, I., & Ohashi, T. 2009, [PASJ](#), **61**, 291
- Yun, M. S., Ho, P. T. P., & Lo, K. Y. 1994, [Natur](#), **372**, 530
- Zschaechner, L. K., Rand, R. J., Heald, G. H., Gentile, G., & Kamphuis, P. 2011, [ApJ](#), **740**, 35